Wetting Across the Lyophilic–Lyophobic Spectrum: Morphological Tuning of Anode Catalyst Layers for the Alkaline Oxygen Evolution Reaction

*Adarsh Jain, Christian Marcks, Gereon Mahler, Ahammed Suhail Odungat, Lars Grebener, Jacob Johny, Mohit Chatwani, Abhishek Shaji, Tobias Melchert, Marc Frederic Tesch, Malte Behrens, Anna K. Mechler, Vineetha Vinayakumar, Doris Segets**

A. Jain, L. Grebener, A.S. Odungat, M. Chatwani, A. Shaji,
Dr. V. Vinayakumar, Prof. Dr.-Ing. D. Segets
Institute for Energy and Materials Processes – Particle Science and Technology (EMPI-PST)
University of Duisburg-Essen
Carl-Benz-Straße 199, 47057 Duisburg (Germany)
E-mail: doris.segets@uni-due.de

Dr. V. Vinayakumar, Prof. Dr.-Ing. D. Segets
Center for Nanointegration Duisburg-Essen (CENIDE)
University of Duisburg-Essen
Carl-Benz-Straße 199, 47057 Duisburg (Germany)

C. Marcks, Prof. Dr. A. K. Mechler
Electrochemical Reaction Engineering
RWTH Aachen University
Forckenbeckstraße 51, 52074 Aachen (Germany)

G. Mahler, T. Melchert, Prof. Dr. M. Behrens
Institute of Inorganic Chemistry
Christian-Albrechts-Universität zu Kiel
Max-Eyth-Straße 2, 24118 Kiel (Germany)

Dr. J. Johny, Dr. M. F. Tesch
Heterogeneous Reactions
Max Planck Institute for Chemical Energy Conversion
Stiftstr. 34-36, 45470 Mülheim an der Ruhr (Germany)

Keywords: Ni-Fe-LDH, wettability, Wenzel model, Cassie-Baxter model, super-hydrophilicity, super-hydrophobicity, alkaline water electrolysis

In alkaline water electrolysis (AWE), anode wettability plays a critical role in governing bubble dynamics at the anode–electrolyte interface. Effective bubble management is essential for improving AWE performance, as it enhances active site accessibility and reduces transport resistance. This study investigates the influence of super-lyophilicity and super-lyophobicity of spray-coated nickel iron layered double hydroxide (Ni-Fe-LDH) anodes on the electrochemical performance for the oxygen evolution reaction (OER). Surface wettability is adjusted through binder selection (Sustainion and Nafion) and drying-induced morphological modifications. Sustainion-based anode layers display pronounced super-lyophilicity ($\theta < 10$ °) governed by the Wenzel model. In contrast, Nafion-based films exhibit tailored super-lyophobicity ($\theta > 150$ °), indicative of a Cassie–Baxter-type wetting state. The super-lyophilic anodes achieve the lowest overpotential, with a reduction of 73 mV at 100 mA cm^{-2} compared to the super-lyophobic anode. Post-electrochemical analysis reveals a correlation between wetting states and the extent of the anode's active area utilization. Super-lyophilic anodes achieve a complete wetting and full layer contribution, while super-lyophobic anodes exhibit large non-wetted regions as high as ~ 47 %, resulting in partial contribution to the OER. The understanding gained by this work enables rational design of high-performance anodes through systematic control of wettability.

1. Introduction

Water electrolysis powered by renewable electricity represents a cornerstone technology for green hydrogen production, yet persistently high energy requirements increase the resulting hydrogen price.[1] While significant research has focused on developing advanced catalysts to reduce oxygen evolution reaction (OER) overpotentials, the critical role of gas-liquid-solid contact lines and interfacial phenomena, and particularly the role of the anode wettability remains inadequately addressed despite its profound impact on the resulting electrolyzer efficiency.[2] This is because, at the anode surface, complex interactions between electrolyte penetration, oxygen bubble nucleation, and detachment dynamics directly influence active site accessibility, mass transport limitations, and ultimately system performance.[3]

Wettability is a well-known and extensively researched topic in the branch of fluid dynamics, particularly in the fields of self-cleaning surfaces, biotechnology, medicine, and material

engineering.[4] In the context of water electrolysis, many researchers have studied wettability in relation to porous transport layers or gas diffusion layers to better understand multiphase fluid transport phenomena.[5] For instance, Iwata et al.[6] specifically investigated wettability in AWE using a Ni-PTFE coating electrodeposited on a 95 % porous Ni foam. Similarly, Heinrich et al.[7] analyzed oxygen bubble nucleation on hydrophilic and hydrophobic surfaces, showcasing that significantly quicker nucleation processes take place for the latter case. Furthermore, Krause et al.,[8] as well as Sakuma et al.[9] have shown the influence of the wetting state on bubble size and bubble coverage of the anode, thus, strongly impacting the OER performance.

The contact angle (θ) between the electrolyte and the anode surface serves as a key descriptor of surface wettability. Depending on the anode surface and electrolyte properties, the anode exhibits either lyophilicity (θ between 0 to 90 °, aerophobic), or lyophobicity (θ between 90 to 180 °, aerophilic), influencing the electrolyte infiltration, bubble nucleation, growth, and detachment.[10] Here, the term *lyophilicity/lyophobicity* is used instead of *hydrophilicity/hydrophobicity* because the electrolyte consists of more than just water. At the extreme ends of this spectrum, super-lyophilic surfaces (θ between 0° and 10°) enable near-complete wetting, while super-lyophobic surfaces (θ between 150° and 180°) will lead to near-no wetting.[11] These interactions are commonly interpreted using physics-derived models such as Young's, Wenzel's, and Cassie-Baxter's models.[12] In brief, Young's model describes the contact angle θ on a flat surface. In contrast, the Wenzel and Cassie–Baxter models apply to rough, porous and hierarchically structured surfaces. In practice, catalyst layers often exhibit a distinct morphology with pore networks underneath. The Wenzel model is generally associated with a lyophilic behavior of the surface under investigation, where the liquid fully penetrates surface textures. The Cassie–Baxter model corresponds to a lyophobic wetting state, where the liquid resides atop surface structures while air remains entrapped within the underlying cavities. In some cases, the surface structures exhibit transitional states between these classical regimes, i.e., described by the Cassie-Wenzel model, creating opportunities for strategic wettability engineering.[13]

In our previous study, we demonstrated how morphological features translate into wetting behavior and ultimately influence OER performance.[14] However, that work focused exclusively on anodes exhibiting lyophobic characteristics. In this study, we complete the wettability spectrum—from super-lyophilic to super-lyophobic surfaces—and establish a

direct link between surface wettability, its description via the Wenzel and the Cassie-Baxter model, and the resulting two-phase flow dynamics. This includes both the spreading of the alkaline electrolyte on the anode surface, as well as the drainage of oxygen bubbles from the catalyst layer. Therefore, we systematically adjusted the wettability of nickel–iron layered double hydroxide (Ni-Fe-LDH) catalyst layers. To achieve this, we incorporated two ionomers with distinct wetting characteristics: the commonly used lyophilic Sustainion (a fluorine-free hydroxide ion conducting polymer) and the lyophobic Nafion (a fluorine-containing ionomer originally designed for proton conduction) into catalyst ink formulations that were used for catalyst layer fabrication by spray-coating.[15] To further modify the morphology of the catalyst layers at constant chemical composition, drying temperatures of 50 °C and 150 °C were applied, in line with our previously developed methodology.[14] Through comprehensive characterization of morphology, chemical properties, mechanical strength, wettability, and electrochemical performance, we establish a relationship between wettability and interfacial flow dynamics during OER. This framework provides precise control over anode-electrolyte-oxygen interactions, ultimately enabling to understand and fully exploit the wetting mechanism of anode layers for alkaline water electrolysis (AWE).

2. Results and Discussion

2.1 Catalyst synthesis and assessment

The catalyst material used in this study, Ni-Fe-LDH nanosheets, was synthesized via a pH-controlled precipitation method, following the synthesis parameters reported by Haase et al.[16] for cobalt iron (CoFe)-LDH (see Experimental Section for details).

Figure 1 presents the structural and elemental characterization of Ni-Fe-LDH nanosheets. The X-ray diffraction (XRD) pattern (a) exhibits the characteristic diffraction peaks corresponding to the (003), (006), (012), (101), and (015) planes, confirming the formation of a hydrotalcite-like layered structure for the $Ni_{0.7}Fe_{0.3}$ LDH.[17] The simulated pattern was generated using the ICSD entry 157485 for iron-hydroxycarbonate using parameters from PDF-2 [40-125] for nickel, supporting the phase identification. The broadening of these reflections suggests the presence of small crystallite domains, which is confirmed by transmission electron microscopy (TEM) micrographs in Figure 1b and 1c, that reveal an ultrathin, crumpled, sheet-like morphology with lateral dimensions at the order of 100 nm and sheet thicknesses around a few nanometers. The high-angle annular dark field scanning transmission electron microscopy (HAADF-STEM) image in Figure 1d further confirms the nanosheet structure.

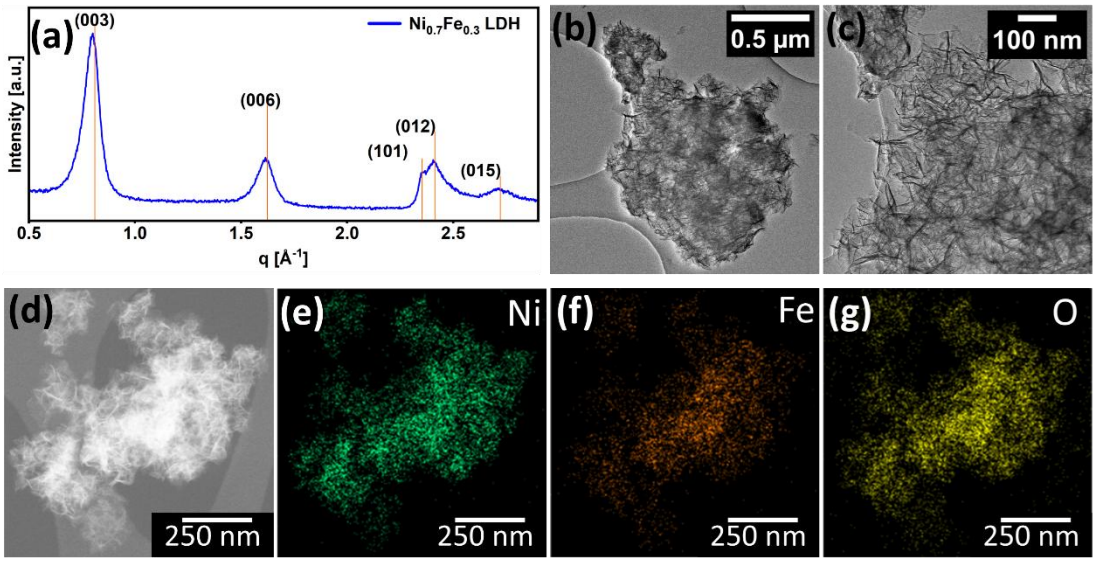

Figure 1. Structural and compositional analysis of Ni-Fe-LDH nanosheets. (a) XRD pattern of Ni-Fe-LDH showing the characteristic reflections corresponding to the LDH phase, (b, c) TEM images at low (10 kx) and high magnification (30 kx), (d) HAADF-STEM image highlighting the nanosheet structure, (e–g) EDX elemental mapping images demonstrating the homogeneous presence of Ni (green), Fe (orange), and O (yellow).

Elemental mapping via energy-dispersive X-ray spectroscopy (EDX) in Figure 1e–g demonstrates the homogeneous distribution of Ni, Fe, and O throughout the aggregates of nanosheets, indicating uniform composition. The Ni-Fe ratio was confirmed to be 70/30 *via* Inductively Coupled Plasma Optical Emission Spectrometry (ICP-OES, see section S4 for further information).

2.2 Morphology formation and characterization

2.2.1 Catalyst ink properties

This section evaluates the sedimentation of catalyst particles in the continuous phase of the developed inks. Figure 2 illustrates the sedimentation behavior of Ni-Fe-LDH particles under a relative centrifugal acceleration (RCA) of 734 in a water-ethanol mixture as the continuous phase, tested without binder, as well as with the two binders, Sustainion and Nafion. The molecular structure of both binders is provided in Supplementary Figure S1. Additionally, the corresponding transmittograms and stability trajectories are given in Figure 2. In brief, transmittograms are a direct visualization method used to monitor sedimentation dynamics under centrifugal force, while the stability trajectory (S-score) quantitatively tracks this behavior.[18] This approach captures the spatial and temporal evolution of light transmission

through the measuring cell, offering a clear depiction of particle migration, agglomeration, and settling over time.[19]

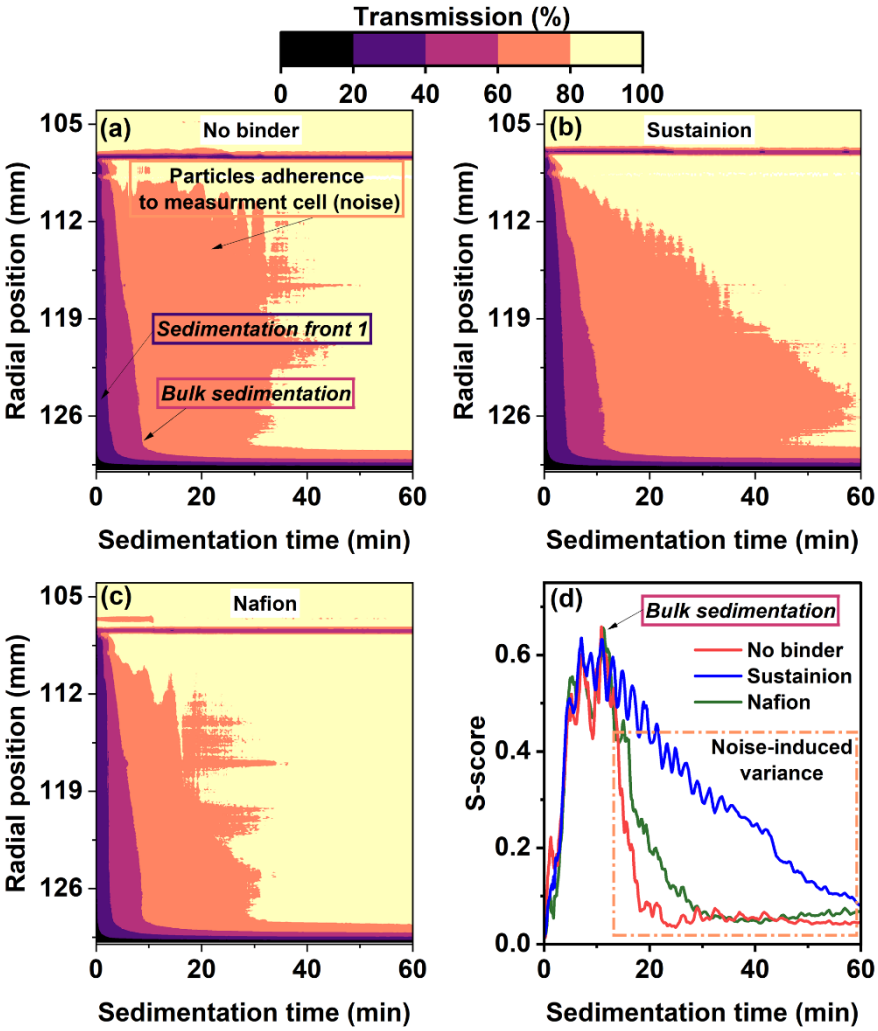

Figure 2. Visualization of the time-resolved sedimentation process via transmittograms: Catalyst particles were dispersed in a mixture of water and ethanol as continuous phase (1:1 ratio) and (a) without binder, with (b) Sustainion, and (c) Nafion as binder. (d) Direct comparison of all inks via stability trajectories.

The transmittograms depicted in Figure 2a–c highlight key features such as different sedimentation fronts, bulk settling, and particle adherence to the measuring cell. In all three cases, the majority of particles settle after approximately 12 min at the given RCA of 734, corresponding to an equivalent of 6 days and 3 h under stationary conditions (RCA = 1). Therefore we can conclude that in line with our previous work, in the presence of the water–ethanol mixture, agglomeration of the catalyst particles is clearly reduced in comparison to pure water or pure ethanol as continuous phase.[14]

To further quantify the similarities in sedimentation behavior, the stability metrics represented by the S-score was employed as shown in Figure 2d. This analysis confirms that all samples exhibit nearly identical bulk sedimentation times, as also observed in the transmittograms.

The incorporation of Nafion or Sustainion into the water–ethanol ink does not alter the colloidal stability of the catalyst, viscosity and surface tension of the ink, indicating that the sedimentation behavior is governed by the continuous phase. This further suggests negligible adsorption of Nafion and Sustainion onto the catalyst surface at the tested compositions and within the time frame of the measurements, as discussed in detail in Section S1 (Supporting Information). While polymeric binders often influence dispersion stability through physisorption or chemisorption,[20] no such interaction was evident in this system.

After thorough characterization, all two inks were deposited on Ni plates (Ni99.2) to obtain layers with different morphologies. For this purpose, we employed coating conditions similar to those described in our previous work.[14]

2.2.2 Morphology of anode layers

Figure 3 provides a detailed comparison of the surface morphology of spray-coated anode layers formulated with either Sustainion or Nafion binders and dried at two temperatures (50 °C and 150 °C). However, it was found that the inclusion of a polymeric binder was essential to tune wettability and to ensure cohesion within the catalyst layer and adhesion to the support because binder-free anodes were not sufficiently mechanically stable. Anodes prepared with Sustainion are denoted here as S-50C and S-150C for drying temperatures of 50 °C and 150 °C, respectively, while those prepared with Nafion are labeled as N-50C and N-150C. The morphology analysis includes scanning electron microscopy (SEM), atomic force microscopy (AFM), mercury intrusion porosimetry (MIP), and focused ion beam scanning electron microscopy (FIB-SEM).

The first and foremost observation is the poor reproducibility of the S-50C anode layer, which exhibited inconsistent macroscopic features across repeated coatings, as shown in optical microscope images at 20x magnification in Figure S3a (Supporting Information). In contrast, S-150C, N-50C, and N-150C coatings were macroscopically uniform and reproducible. Accordingly, SEM imaging of S-50C in Figure 3a (150 x, 2 kx inset image) revealed large cracks and incomplete coverage with LDH particles, with regions of exposed support surface

(highlighted by red circle and arrow). This is a clear evidence of poor film formation. These deficiencies were not observed in the S-150C (Figure 3b) or Nafion-based coatings (Figure 3c and Figure 3d), which all exhibited continuous and macroscopic defect-free surfaces.

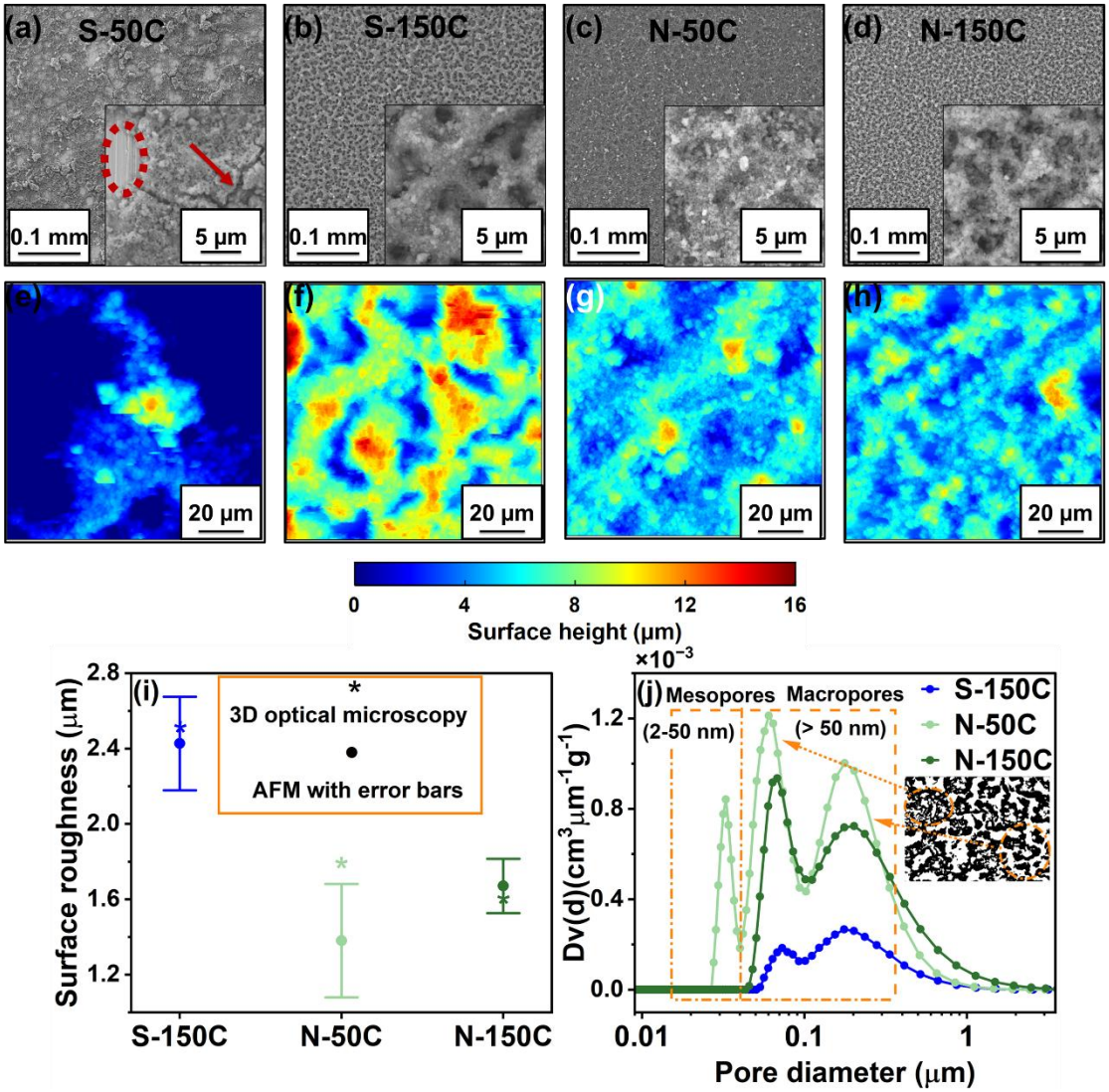

Figure 3. Morphological analysis. Top-view SEM images: (a) S-50C, (b) S-150C, (c) N-50C, and (d) N-150C. Topographical AFM images: (e) S-50C, (f) S-150C, (g) N-50C, and (h) N-150C. Quantitative surface features: (i) root mean square (RMS) surface roughness obtained from AFM (spheres with error bars) and 3D optical microscopy (values marked with *), and (j) pore structure analysis using MIP along with the pore structure captured using FIB-SEM imaging of N-150C.

AFM imaging further emphasized binder- and temperature-dependent differences in the surface topography. S-50C did not exhibit any coherent surface architecture, underscoring the inadequacy of low-temperature processing for Sustainion-based inks. In contrast, the S-150C coating showed similar concave hemispherical features, though they were more pronounced.

N-50C exhibited discrete island-like features, while increasing the drying temperature to 150 °C (N-150C) resulted in the formation of smoother, concave hemispherical structures. This finding is consistent with the morphologies we previously observed in coatings made of commercial nickel cobalt oxide nanoparticles (NCO) at these conditions.[14] As shown in Figure S3e (Supporting Information), depicting catalyst-free coatings made of binder and continuous phase, the Sustainion molecule remains highly mobile at 50 °C, spreading extensively across the Ni support before the solvent evaporates, and consequently agglomerates at the edge of the Ni support. This behavior was not observed for coatings made of pure Nafion under similar conditions, where the binder was distributed homogeneously across the Ni surface. This uncontrolled redistribution in case of S-50C likely prevents uniform catalyst deposition and contributes to the structural irregularities of S-50C. At this stage, due to its poor morphology and reproducibility, S-50C was excluded from further analysis.

Figure 3i presents surface roughness measurements derived from the multistage data quantification (MSDQ) framework for representative characterization,[21] which we developed to extrapolate localized surface features to statistically relevant larger areas (details can be found in the supporting information). The S-150C coating displayed the highest roughness (~2.7 μm), while both Nafion-based layers remained below ~1.7 μm. However, in some regions, surface roughness could not be measured due to pronounced topographical features and limitations of the AFM device. Therefore, to ensure accuracy, the results were validated using a 3D optical profilometer as highlighted in Figure 3i. These findings indicate that the Sustainion-based coating prepared and dried at 150 °C increases the surface roughness. MIP analysis (Figure 3j) revealed that only N-50C exhibited both mesopores (2–50 nm) and macropores (> 50 nm), while N-150C and S-150C were predominantly macroporous. All coated layers consistently showed two characteristic peaks at ~70 nm and ~200 nm in the macroporous domain.

Taken together, these results demonstrate that the drying temperature is not the only factor that determines the film formation.[22] The type of binder that then governs binder mobility and its interaction with the Ni support during drying is equally critical. These findings highlight the importance of carefully analyzing drying protocols and ink compositions when polymeric binders in water-rich inks are used. Following the analysis of morphology formation, the influence of layer composition and morphology on anode layer properties is

explored. A detailed evaluation of this relationship is presented after the chemical characterization of the anode layers as shown in the subsequent section.

2.2.3 Chemical characterization of anode layers

The surface chemical states and molecular structure of S-150C, N-50C, and N-150C anode layers were investigated and compared to each other by employing X-ray photoelectron spectroscopy (XPS) and Raman analysis (Figure 4).

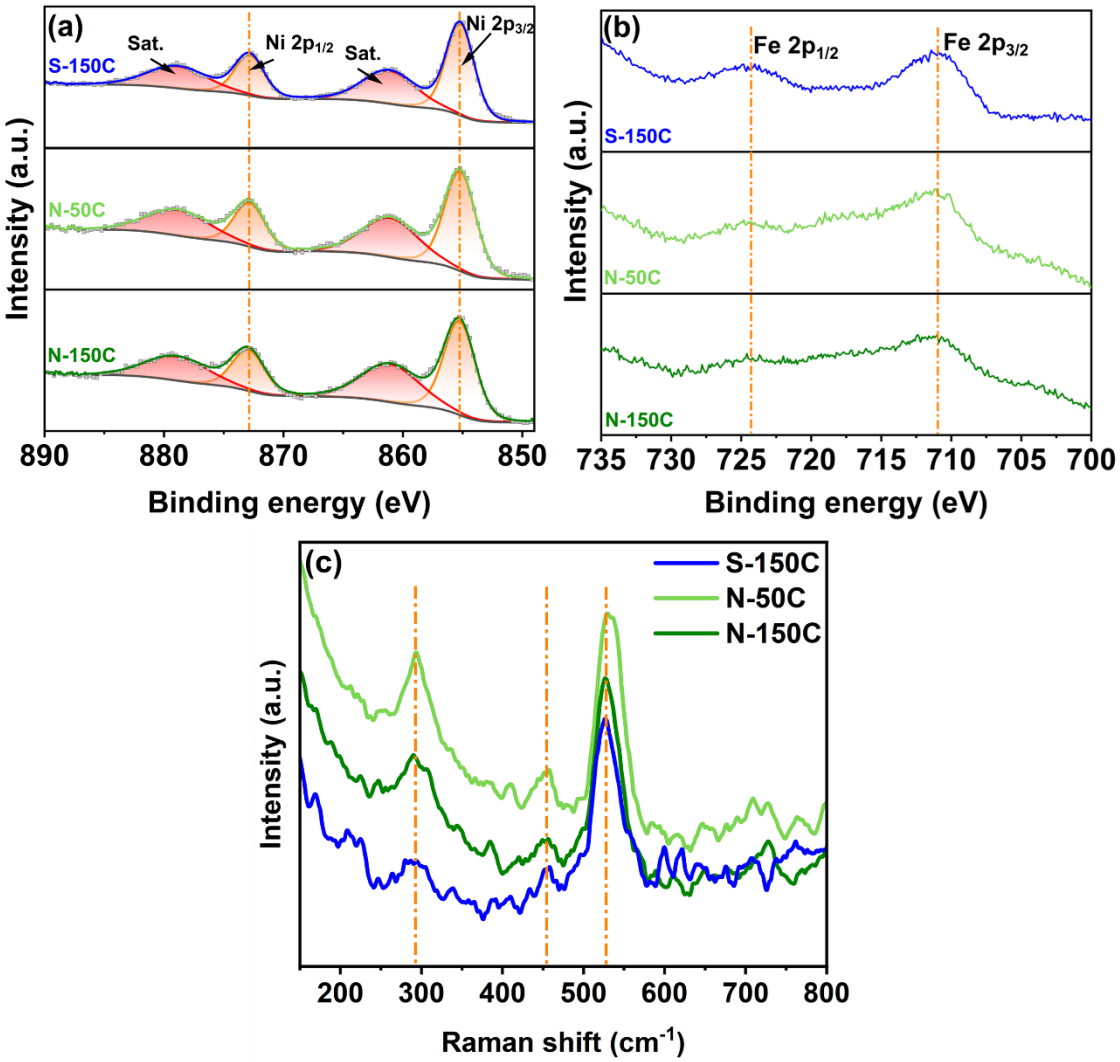

Figure 4. XPS high-resolution (a) Ni2p and (b) Fe2p peaks of S-150C, N-50C, and N-150C anode layers. (c) Raman analysis of the anode layers.

The high-resolution Ni2p peak in all three layers were deconvoluted into the respective $2p_{3/2}$ and $2p_{1/2}$ contributions along with the associated satellite peaks as shown in Figure 4a. The $Ni2p_{3/2}$ peaks located at a binding energy of 855.2 eV and the $Ni2p_{1/2}$ peaks at 872.8 eV correspond to Ni^{2+} in Ni-Fe-LDH.[23] The associated satellite peaks of $2p_{3/2}$ (861.1 eV and

$2p_{1/2}$ (878.9 eV) further validate the desired chemical state of Ni in the anode layers. In comparison to the Ni2p peaks, the Fe2p high-resolution spectra in the anode layers were less intense (Figure 4b). However, the approximate peak locations at 711.0 eV ($2p_{3/2}$) and 724.3 eV ($2p_{1/2}$) in all samples are ascribed to Fe^{3+} in Ni-Fe-LDH.[23] Altogether, the XPS analysis of the Ni-Fe-LDH anode layers suggests a similar surface chemical state in all three layers. Raman spectroscopy was conducted on the layers to identify their characteristic vibrations and compare the molecular structure. The S-150C, N-50C, and N-150C layers exhibit three major Raman bands located at 292, 454, and 527 cm^{-1} corresponding to brucite-like structures of the anode layers,[24] and confirm the same molecular structure in all samples. XPS and Raman analyses collectively evidence that the chemical composition of the coated layers remains consistent across all samples, irrespective of variations in binder type and substrate temperature. This chemical uniformity across the anode layers ensures that any differences observed in their electrochemical performance can be attributed primarily to morphological and macroscopic property variations, allowing for a fair comparison.

2.3 Macroscopic properties of anode layers

In this section, we evaluate the macroscopic properties of the anode layers, specifically their mechanical stability and wettability. Both are important, as a higher mechanical strength contributes to reduced contact resistance,[14] and the initial interaction with the electrolyte (1 M KOH) defines the wetting regime. For instance, lyophobic surfaces can facilitate bubble formation and removal. As clearly shown in our previous work,[14] these macroscopic anode layer properties are therefore essential as a link to assess and understand the relation between anode composition and morphology with the overall anode performance.

2.3.1 Adhesion analysis

Figure 5 presents the results of a centrifugal detachment test designed to evaluate the interfacial mechanical strength between the catalyst layer and the Ni support. The test setup involved a sandwich structure where an anode was adhered to a steel backing plate, and a circular copper test mass was affixed on top using adhesive glue.[25] The assembly was mounted onto a centrifugal detachment device, where an increasing centrifugal force was applied until failure occurred. The test was terminated when the copper test mass impacted the detector plate, triggered either by i) adhesive failure at the interface between the Ni support and the catalyst layer, ii) cohesive failure within the catalyst layer, or iii) failure at the

interface between the adhesive and the catalyst layer, indicating anodes of high mechanical stability.

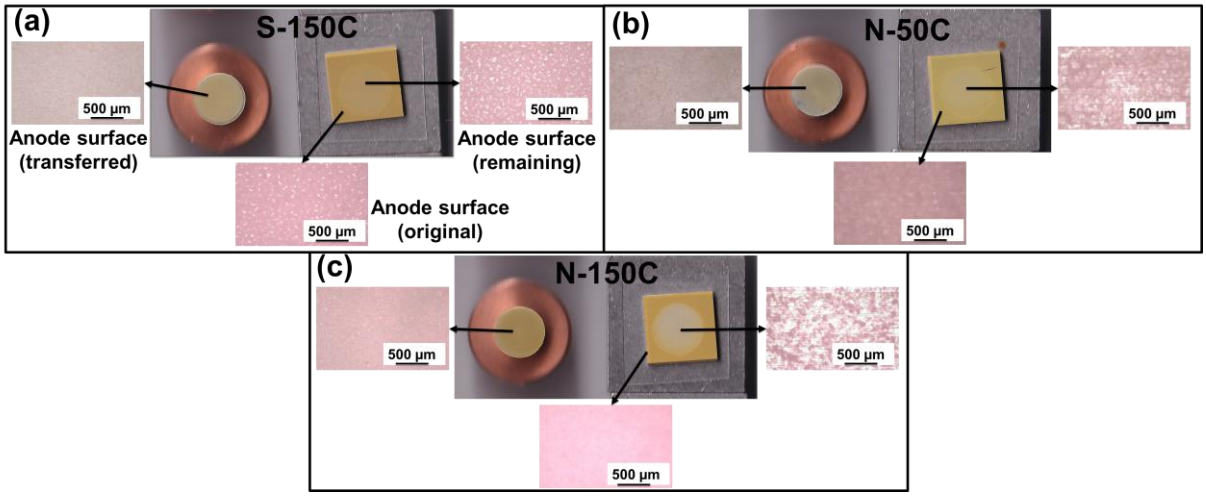

Figure 5. Adhesion analysis of spray-coated anode layers via centrifugal detachment testing: (a) S-150C, (b) N-50C and (c) N-150C.

The central images in 5a-c show the complete test configuration post-failure, while the accompanying micrographs display the original anode surface (bottom), the catalyst layer transferred onto the adhesive on the copper mass (left), and the remaining surface on the Ni support (right). Surface analysis after the centrifugal-detachment-testing confirmed partial cohesive failure in all three cases, as evidenced by material transfer to the copper adapter (left inset) and residual catalyst on the Ni support (right inset) in Figure 5. This indicates that the adhesion between catalyst and Ni support is stronger than the cohesion between the catalyst particles. Among the tested anodes, S-150C demonstrated the highest mechanical strength of 0.69 ± 0.16 MPa, showing a homogeneous and dense, mechanically stable layer. In contrast, N-50C and N-150C exhibited significantly lower strengths of 0.25 ± 0.11 MPa and 0.17 ± 0.07 MPa, respectively, with irregular surface features and patch-like marks on the Ni support caused by catalyst detachment.

Although particle interactions in the ink were comparable for both binders, we hypothesize that the enhanced mechanical strength observed with Sustainion arises from its more uniform distribution, as shown in Figure S3b and f. This uniformity leads to a more even distribution of mechanical stress and, thus, strain under tensile loading. In contrast, the increased surface roughness and porosity observed in the Nafion-containing samples suggest that mechanical forces become locally concentrated, which may contribute to their reduced adhesion. This

relationship between morphological uniformity and mechanical integrity will be explored in greater detail in future work.

2.3.1 Wettability analysis

As the second key factor under investigation to assess anode layer properties, wettability was analyzed to understand how the electrolyte interacts with the textured anode surfaces. Static contact angle measurements are widely used to quantify the wetting behavior, but they become unreliable when surface interactions fall at the extremes of the lyophilicity/lyophobicity spectrum. In this study, anodes exhibited either super-lyophilic ($\theta < 10$ °) or super-lyophobic ($\theta > 150$ °) characteristics, making it impractical to report consistent or meaningful contact angle values. To overcome this limitation, high-speed imaging was employed to capture the dynamic spreading behavior of 1 M KOH droplets on the spray-coated surfaces. An accompanying analytical framework was developed using ImageJ software to process the time-resolved droplet shape evolution, offering a more comprehensive view of the wetting dynamics beyond static endpoints. Figure 6 shows the normalized height of the droplet relative to the initial droplet tip over time, along with corresponding snapshots of the droplet morphology at key time points. This dynamic analysis provides insight into the early stage wetting regime, offering clues about the interfacial interaction between the electrolyte and the textured anode surface.

In the case of the S-150C anode (Figure 6a), the droplet undergoes rapid spreading and height reduction, eventually stabilizing into a highly flattened state. This behavior reflects a strong interaction between the droplet and the surface, consistent with a Wenzel wetting regime, in which the liquid fully penetrates the rough and porous structure. This outcome is indicative of a super-lyophilic behavior, with enhanced electrolyte contact, stronger liquid adhesion on the surface and gliding of the electrolyte through the pore network. In contrast, in case of N-50C (Figure 6b), the droplet clearly bounces, by undergoing a first rebound, a secondary rebound, and a series of minor hops before its final settling. With regard to its areal spread, the droplet does not spread significantly and maintains a high apparent θ throughout the interaction. These observations are consistent with a Cassie–Baxter wetting state, where the droplet rests on top of trapped air pockets within the morphology, indicative of a super-lyophobic surface.

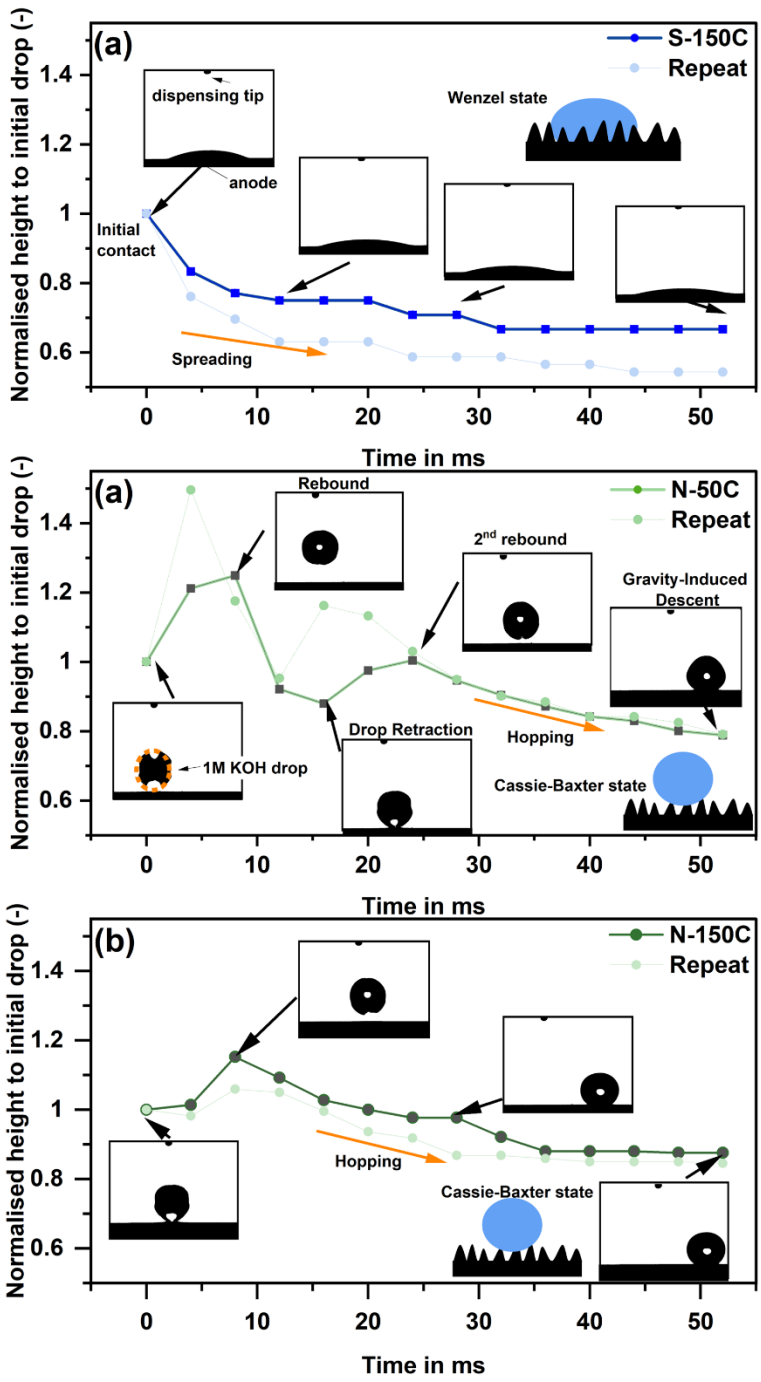

Figure 6. Dynamic wettability analysis of spray-coated anode layers capturing the impact of 1 M KOH via high-speed imaging: (a) S-150C which displays immediate spreading, characteristic of a super-lyophilic surface following the Wenzel wetting model. (a) N-50C, which exhibits multiple rebounds followed by retraction and hopping, indicative of pronounced lyophobicity and a Cassie–Baxter wetting state. (b) N-150C, which shows reduced rebound and delayed retraction, consistent with a less pronounced Cassie–Baxter regime compared to N-50C.

For N-150C (Figure 6c), a similar sequence is observed, though with slightly dampened rebound heights and reduced hopping. The wetting state remains in the Cassie–Baxter regime, but the slightly reduced repellency compared to N-50C is attributed to the altered morphology and the missing presence of mesopores. The droplet shows reduced kinetic energy dissipation, but still maintains a non-wetting behavior, which is characteristic of super-lyophobicity. Overall, the comparison of both Nafion-based anodes indicates that N-50C exhibits a higher degree of lyophobicity than N-150C.

We attribute this behavior to two main factors: the inherent wetting characteristics of the binders utilized, and the binder- and drying-induced morphology.

First, the intrinsic wetting properties of the binders play a key role in defining the wettability of the layer. Sustainion consists of a hydrophilic polymer backbone (see also Figure S1a),[26] which strongly contributes to the super-lyophilic wetting mechanism for S-150C. Nafion contains both hydrophobic and hydrophilic phase-separated structural segments (see also Figure S1b),[27] but exhibits high hydrophobicity due to the presence of perfluoroalkyl groups.[28] Therefore, even though the Ni-Fe-LDH catalyst employed across all samples possesses inherent hydrophilicity due to its interlayer water content,[29] the dominant wetting behavior of the layers is still governed by the binder molecule.

Second, morphological features such as roughness and pore network, resulting from ink formulation and drying conditions play a crucial role in determining wettability. On the one hand, S-150C exhibits the highest surface roughness among all investigated anodes, yet its wettability remains largely unaffected by its morphology, highlighting the dominant influence of the employed binder molecule. On the other hand, N-50C exhibits an island-like surface morphology containing both mesopores and macropores, contributing to its pronounced super-lyophobic behavior. In contrast, N-150C displays a concave hemispherical morphology with a predominantly macroporous structure, resulting in slightly reduced repellency. Here, the role of morphology becomes evident: although both are fabricated with the same binder (Nafion), differences in morphology lead to distinct droplet impact and rebound behaviors.

Thus, it is the interplay between intrinsic binder wettability and the binder-mediated morphology that ultimately determines whether a layer exhibits super-lyophilic or super-lyophobic behavior. This comparison underscores the distinct, yet complementary roles of

surface chemistry and morphology as the two decisive factors in governing wetting dynamics. The layer properties are summarized in Table 1, highlighting the combined influence of binder type and morphology on wettability and mechanical strength. The corresponding implications of these layer properties on the electrochemical performance for oxygen evolution are examined in the subsequent section.

Table 1. Anode layer properties: Measured wettability and mechanical strength for S-150C, N-50C and N-150C.

Properties	S-150C	N-50C	N-150C
Mechanical strength/ MPa	0.69 ± 0.16	0.25 ± 0.11	0.17 ± 0.07
Mechanical failures	Partially cohesive	Cohesive	Cohesive
Wettability	Super- lyophilic	Super-lyophobic	Super-lyophobic
Droplet mobility	Spreading	Rebounding	Bouncing

2.4 Electrochemical performance of anode layers

Electrochemical characterization was carried out using a 3-electrode beaker-cell setup, adjusted for plate anodes from the work presented by Thissen et al.[30] A detailed description of the measurement protocol can be found in Section S4 (Supporting Information).

Figure 7a shows the uncompensated resistance (R_u) values for each anode layer measured at three stages: before stability testing, after 8 hours of OER, and after the final activity assessment. As the electrode arrangement and electrolyte was consistent throughout all experiments (and especially within one experiment), contributions to R_u from the ionic resistance of the electrolyte can be assumed to be constant. Thus, any variations of R_u are ascribed to changes at the electrolyte-catalyst-support interfaces. The S-150C sample consistently demonstrates the lowest and most stable R_u values, indicating improved interfacial conductivity. In contrast, N-50C and N-150C exhibit higher and more variable R_u values, suggesting larger contact resistance at the electrolyte-catalyst-support interfaces. Figure 7b presents cyclic voltammetry (CV) profiles during anode conditioning, showing the 5^{th} and 50^{th} cycle, revealing differences in the development of the surface charge during conditioning. All anodes show a notable increase in passed surface charge during cycling, indicating the formation of the active oxyhydroxide phase.[31] However, the S-150C anode achieves significantly higher current densities compared to the Nafion-based anodes, suggesting better utilization of the catalyst, due to the high accessibility of the electrolyte for the Sustainion-based layers.

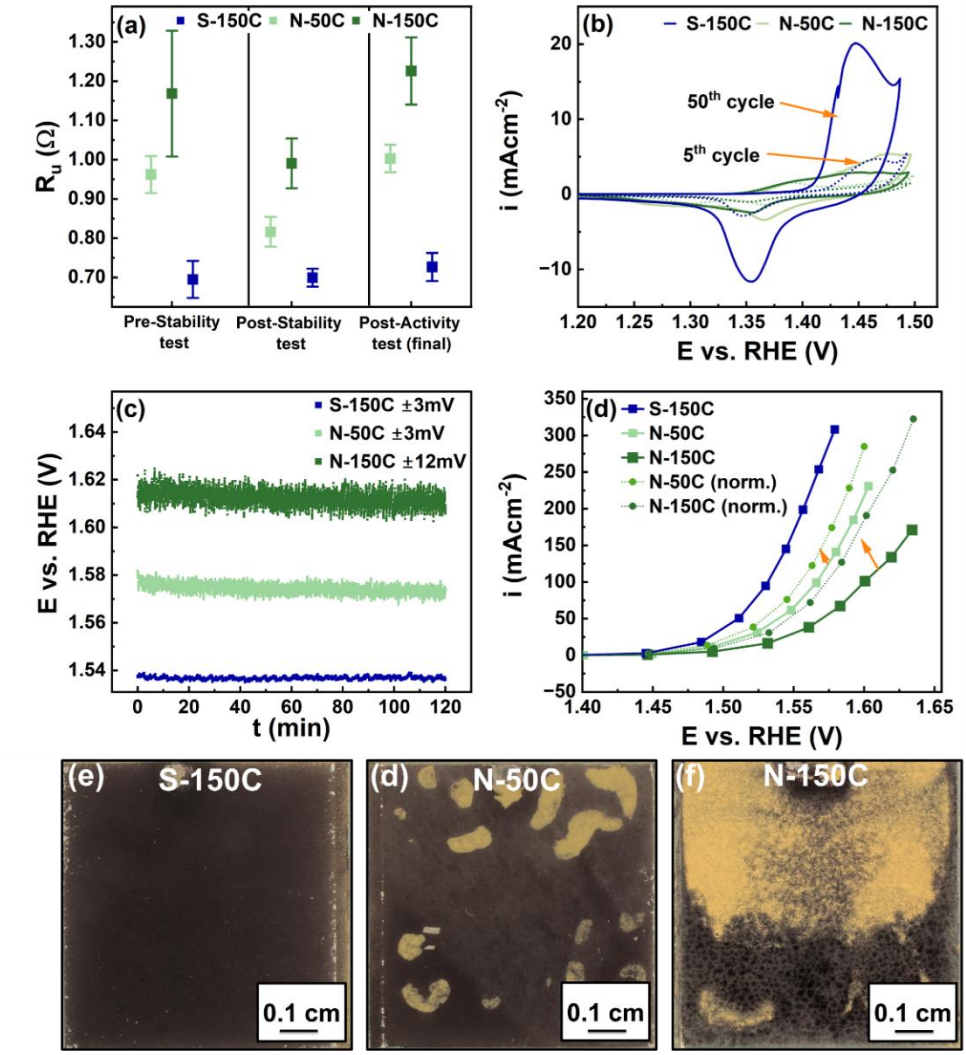

Figure 7. Electrochemical characterization of spray-coated anode layers: (a) R_u measured at open-circuit potential before stability testing, after stability testing, and after the final activity measurement, reflecting changes at the electrolyte–anode and layer–support interface. (b) Conditioning CV curves of the 5th and 50th conditioning cycle. (c) CP stability measurement over 2 h at 100 mA cm^{-2} with the standard deviation calculated by a triple determination. (d) Final OER activity curves after stability testing along with the same data normalized on the wetted area. Optical images of the anodes post-OER for (e) S-150C, (f) N-50C, and (g) N-150C. All measurements were performed in 1 M KOH at room temperature (RT).

Figure 7c displays the short-term stability measurement via chronopotentiometry (CP) for 2 h at 100 mA cm^{-2}. We calculated the average absolute deviation of the potential fluctuations, to quantify the effect of bubble formation on the anode surface. The potential trace for S-150C remains remarkably stable, fluctuating by ~0.4 mV. In comparison, N-50C and N-150C show larger fluctuations of ~1 mV and ~2 mV, respectively. We attribute these fluctuations to gas

bubbles adhering to the anode surface, which dynamically alter the active surface area and, consequently, the measured potential. Among the two Nafion-based anodes, N-50C exhibits lower noise, whereas the pronounced noise observed in N-150C suggests increased bubble accumulation, leading to greater variations in the active surface area. As can be seen from Figure 7c (stability) and Figure 7d (stationary polarization), the activity follows a clear trend: S-150C > N-50C > N-150C, with the potential at 100 mA cm^{-2} (E_{100}), after a total of 8 h of stability CP measurement, of 1.536 V, 1.573 V and 1.609 V, respectively. We attribute the observed performance trends and differences during electrode conditioning to variations in wettability and the intrinsic properties of the binders used. Post-OER optical microscopy (Figures 7e–g, 20x magnification) confirms macroscopic wetting differences in such way that yellow regions indicate areas that remained unwetted and thus inactive during operation, while dark regions correspond to oxidized, wetted areas. Accordingly, the S-150C anode (Figure g) demonstrates superior performance due to its complete wetting.

The extent of the non-wetted regions on Nafion-based anodes was quantified by image analysis (see Experimental section) as 19 ± 4 % for N-50C and 47 ± 4 % for N-150C – an increase of 28 % for the latter. As can be seen in Figure d, normalizing the obtained polarization data to the wetted area clearly enhances the performance of the poorly wetted anodes, though they do not fully overlap. We attribute this to differences in the number of active sites participating in the reaction. Continuous surface oxidation during OER may further alter the surface state, possibly enabling additional wetting through wicking,[32] a fluid transfer mechanism driven by capillary forces in mesopores, which are only present in the N-50C anode. Furthermore, the inherently higher ionic conductivity of the Sustainion ionomer might additionally enhance site accessibility compared to Nafion-based anodes.

In the following section, we try to rationalize the observed electrochemical trends, by further considering the influence of bubble off-surface-transport on performance. Thereby we will also discuss how this is linked to wettability and the three-phase contact line generated by bubble, electrolyte and anode.

2.5 Relationship between single drop wettability and the three-phase-contact line

Our hypothesis is motivated by the interfacial force balance model, which has been presented in literature,[6,33] in which bubble detachment is governed by a competition between buoyancy and surface tension forces at the bubble–catalyst interface. Specifically, when the diameter of

the evolving gas bubble is comparable to, or larger than, the characteristic pore size of the catalyst layer (see Figure 8a-c), its movement is no longer governed by transport through the pore network as described by Darcy's law. Instead, bubble detachment can be approximated by a simplified force balance, as outlined in Equations 1-3 (see Figure S4 for a more detailed depiction of the force balance):

$$F_b = F_s \tag{1}$$

$$F_b = V_b \cdot \left(\rho_{el} - \rho_g\right) \cdot g \tag{2}$$

$$F_s = \gamma \cdot 2\pi L_b \cdot \sin\left(\theta_{gs}\right) \tag{3}$$

Where F_b and F_s is the buoyancy force (N) and surface tension force (N), respectively, V_b the bubble volume (m^3), ρ_{el} and ρ_g the density of electrolyte and oxygen (kg m^{-3}), respectively, g the gravitational constant (m s^{-2}), γ the surface tension (N m^{-1}), L_b the contact perimeter of bubble to anode (m) and θ_{gs} the gas-solid contact angle (°). Please note that the contact angle given here represents the contact angle between bubble and anode, and thus scales inversely to the measured contact angle we have presented until this part of the work.

Considering this relationship, the mode of bubble transport becomes clearer. For S-150C anodes, the small (measured) liquid-solid contact angle results in small bubble detachment diameters (see Figure a) due to a reduced perimeter of the bubble-to-anode-surface and, consequently, small adhesion. This promotes frequent detachment, continuously freeing surface area for the nucleation of new bubbles and thereby maintaining a large active area overall. In contrast, Nafion-based anodes exhibit larger liquid-solid bubble contact angles and wider contact perimeters, which favor sustained bubble growth – often enhanced by coalescence with smaller bubbles,[9,34] – until detachment occurs once buoyancy overcomes adhesion.

The remaining question is why N-50C and N-150C display distinct wetting behaviors after electrochemical testing. As Qin et al.[35] reported, higher lyophobicity results in a more pronounced lateral mobility of gas bubbles, with a minimum in mobility for a contact angle of 90°C. Given the higher lyophobicity of N-50C (see wettability analysis in Section 2.3.1), this anode likely facilitates lateral bubble movement which enables a more frequent bubble coalescence compared to N-150C. This enhanced bubble mobility also clears more surface area by enabling transient wetting, thereby promoting additional bubble nucleation. This observation is consistent with our previous work.[14]

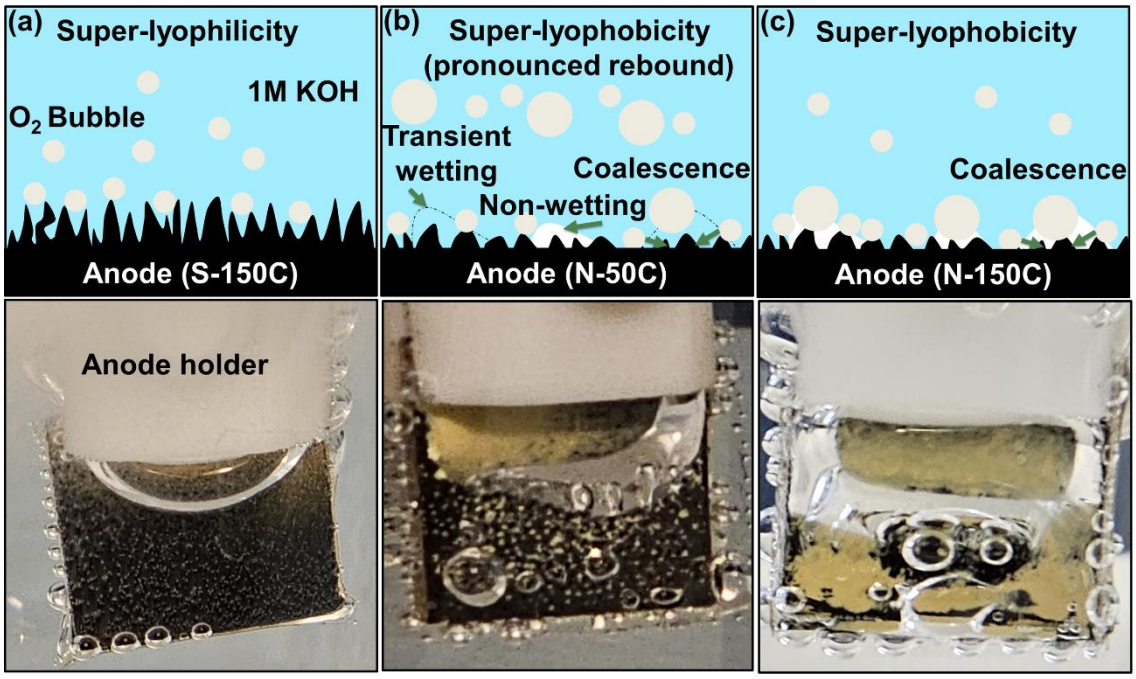

Figure 8. Schematic illustration of bubble evolution during OER, accompanied by photographs of (a) S-150C, (b) N-50C, and (c) N-150C.

Collectively, these results confirm that both, binder chemistry and morphology-driven wettability are critical parameters for optimizing bubble management and, thus, key parameters defining the overall OER performance.

2.6 Transferability of findings and overview

The anode composition–morphology–wettability–performance relationships established here build directly on our previous work with commercial NCO anodes and extend in this study to a lab-synthesized, advanced Ni-Fe-LDH system. Despite differing morphologies – spherical particles for NCO versus nanosheets for Ni-Fe-LDH – spray-coated layers exhibited similar morphologies: island-like surface morphologies at 50 °C and concave hemispherical ones at 150 °C. These features were consistently reproduced for Nafion-based inks. An additional introduction of the inherently lyophilic Sustainion binder enabled us to significantly expand the accessible range of wetting behavior: from super-lyophilicity ($\theta < 10$ °), dominated by binder effects, to super lyophobicity ($\theta > 150$ °), driven by the enhanced surface roughness induced by the nanosheets.

To consolidate these insights, Figure 9 presents a unified framework linking surface wettability with the mass transport behavior monitored during alkaline OER. Anodes

fabricated in this study – S-150C, N-50C, and N-150C – are evaluated alongside previously reported NCO anodes coated at 50 °C and 150 °C (NCO-50C and NCO-150C). These anode features are positioned along a gradient of contact angle (θ), spanning from (super)-lyophilic to (super)-lyophobic regimes, and categorized according to the corresponding wetting states based on classical models: Wenzel, Cassie–Baxter, and the intermediate Cassie–Wenzel transition, each illustrated with representative droplet shapes. This progression is visually represented through a consistent background color gradient—from light to dark green—across all three bars in the figure. In the top bar, lighter shades indicate lower lyophilicity/ lyophobicity, while darker shades reflect increased lyophilicity/lyophobicity. In the lower portion of the framework, the influence of these wetting states on mass transport such as reactant (KOH) accessibility and product transport (O_2) is highlighted.

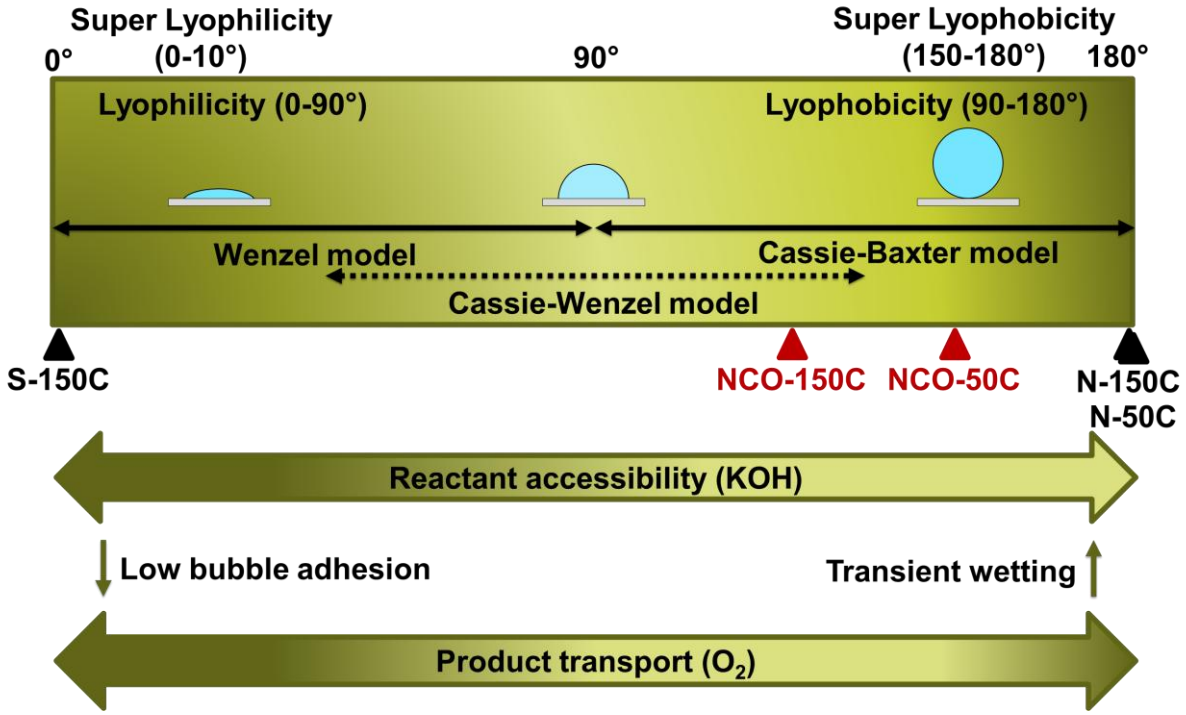

Figure 9. Interplay between surface wettability and mass transport behavior across different anode architectures. Electrodes from our previous work[14] are highlighted in red. Dark shades indicate significantly enhanced relative OER performance, bright shades signify lower relative OER performance.

For reactant accessibility, lyophilic surfaces favor complete electrolyte wetting and access to the catalytic interface, whereas lyophobic regimes hinder electrolyte penetration into the catalyst layer. In the case of product release (O_2 in the form of bubbles), lyophilic surfaces promote fast bubble detachment due to the low adhesion forces, consequently freeing up space for further bubble nucleation. Conversely, on lyophobic surfaces, the larger adhesion

force leads to the growth of larger bubbles and, thus, reduced electrolyte accessibility. Notably, catalytic surfaces exhibiting super-lyophobic behavior once again facilitate the removal of non-polar O_2 gas bubbles, driven by enhanced lateral bubble mobility and coalescence. This enables transient wetting of the anode surface. The performance trends for Ni-Fe-LDH consequently follow those observed in NCO systems, validating the herein established composition–morphology–wettability–performance relationship, across distinct types of electrocatalysts.

Taken together, this framework underscores the critical role of wettability engineering in balancing reactant influx and product drainage. It may also serve as a comparative reference for future anode designs, enabling the broader community to contextualize and rationalize wettability-dependent transport phenomena across diverse catalyst architectures and materials with distinct intrinsic wetting properties. Regarding high-performance anodes for the alkaline OER, we recommend the design of highly lyophilic structures. However, when lyophobic binders are required – for example, to meet mechanical stability demands – the morphology should be engineered through surface roughness and pore network design to shift wettability into the (super-)lyophobic regime. This promotes efficient gas bubble transport and transient wetting.

3. Conclusion

In this study, we demonstrate how ink composition and deposition conditions influence the morphology, wetting state, and electrochemical performance of Ni-Fe-LDH-based anodes for AWE. In contrast to our previous work on NCO anodes, which focused exclusively on lyophobic coatings, the current investigation expands the wetting state spectrum to include both super-lyophobic and super-lyophilic anodes. These states were achieved through the controlled selection of binders. Additionally, morphology and layer properties of anodes are tuned through varying the drying temperature during coating at 50 °C and 150 °C.

Super-lyophilic layers prepared with Sustainion as a binder exhibited complete wetting, consistent with the Wenzel wetting state. However, their coating reproducibility at 50 °C was limited because of the uncontrolled movement of the binder, thereby generating agglomerates at the edge of the Ni support, which hindered uniform layer formation. The S-150C anode combined high surface roughness with a super-lyophilic wetting state, enabling efficient KOH transport and improved catalyst utilization. These combined effects led to superior

electrochemical performance. In contrast, Nafion-based layers showed uniform and reproducible coatings at both 50 and 150 °C, along with tunable super-lyophobicity, consistent with the Cassie–Baxter regime. Within the Nafion-based anodes, N-50C exhibited greater catalyst layer utilization than N-150C, as evidenced by post-OER optical images. This is attributed to its more pronounced super-lyophobicity, which facilitated the detachment of oxygen bubbles during OER.

Overall, this study confirms that the composition–process–morphology–wettability–performance relationships are transferable across different catalyst systems, provided that material-specific behavior is considered. These insights provide a pathway for engineering advanced catalyst layers that optimize KOH accessibility, gas bubble growth and detachment, and mechanical durability in alkaline water electrolysis.

4. Experimental Section/Methods

Catalyst synthesis and Characterization

The Ni-Fe-LDH was synthesized using an automatic laboratory reactor system (Optimax 1001, Mettler Toledo). The reactor was prefilled with 200 mL of deionized water. A total of 120 g of metal salt solution, containing 0.28 M $Ni(NO_3)_2$ (99.9 %, abcr) and 0.12 M $Fe(NO_3)_3$ (99.5 %, Grüssing), was dosed continuously over the course of 1 hour under stirring. The pH was maintained at 8.5 by simultaneous addition of the precipitation agent consisting of 0.6 M NaOH (99 %, org. Laborchemie) and 0.09 M Na_2CO_3 (99.5 %, Grüssing). After precipitation, the suspension was aged in the reactor at 50 °C for 1 hour. The resulting precipitate was washed repeatedly 5 times with deionized water until the supernatant turned orange and its conductivity dropped below 100 µS cm^{-2}, and isolated by centrifugation at 2000 rpm for 3 minutes. The sample was then additionally washed once with ethanol and centrifuged under the same conditions. It was subsequently pre-dried on a filter frit under ambient airflow for 30 minutes, followed by drying in a temperature-controlled chamber at 60 °C in air for 16 hours.

Inductively coupled plasma – optical emission spectroscopy (ICP-OES) analysis was performed using an ICP-OES Avio 200 by PerkinElmer and Powder XRD of the powdered pre-catalyst was conducted at room temperature utilizing a STOE Stadi P device in transmission geometry with Mo-Kα radiation. TEM measurements were carried out on a Jeol JEM 2200 fs microscope (Akishima, Japan) and EDX elemental mappings were acquired with an X-Max 100 detector (Oxford Instruments, Abingdon, United Kingdom).

Anode fabrication and Characterization

For ink preparation, two formulations were prepared using either Nafion™ (perfluorosulfonic acid, 5 % dispersion, D521, Ion Power GmbH) or Sustainion™ (Dioxide Materials) as binders. Deionized (DI) water with a resistivity exceeding 18.1 MΩ·cm, obtained from a Milli-Q system, was mixed with analytical-grade ethanol in a 1:1 volume ratio to serve as the carrier solvent. The binder-to-catalyst (B/C) ratio was maintained at 0.2, and the total solid content was fixed at 1 mg mL^{-1}. The selected binder was first dispersed in the water–ethanol mixture using a sonication bath (Elmasonic S 30 H, Germany) for 5 minutes at room temperature. The catalyst powder was then added, followed by high-energy dispersion using a tip sonicator (Branson SFX550), operated in continuous mode at 40 % amplitude for 6 minutes. An ice bath was used throughout the process to minimize heat generation and prevent particle re-agglomeration. The subsequent steps, including ink characterization, spray-coating, layer characterization, and electrochemical testing, were performed exactly as described in our previous study,[14] and are detailed again in the Supporting Information, Section S4 for completeness. To quantify the extent of non-wetted regions following electrochemical testing, top-view optical images of the anodes were imported into ImageJ. The images were first converted to 8-bit grayscale, and the Otsu thresholding algorithm was applied to achieve binarization. The resulting binary images were analyzed to determine the areal fraction of non-wetted surface, which appeared as bright regions.

Statistical analysis

The initial ink screening was carried out using a DoE approach with two replicates per condition. Two selected ink formulations were subsequently selected for coating on Ni-based substrates, resulting in the fabrication of 40 electrodes (20 for each ink). Morphological characterization was performed individually on each anode, with time efficiency considered during measurement planning. The MSDQ methodology was utilized to extract surface features, ensuring that the data reflected spatial representativeness across the electrode area.[21] Characterization of the anode layer's wettability and mechanical strength was performed using a minimum of two measurements per condition to ensure both reproducibility and statistical relevance. Results are reported as either mean ± SD or as repeated measurements, and are presented in figures or accompanying tables across the manuscript. Electrochemical stability testing was conducted on three separate anodes per condition, and the displayed plots represent average values, with the SD shown as the mean of individual SDs across time points. For CV activity data, a representative electrode was

selected to illustrate the trends clearly. Mean and SD were not included for CV curves, as post-measurement Ru correction introduces shifts in both current and potential axes, making data averaging inappropriate. All statistical analyses were conducted using MATLAB R2022a and OriginPro 2024. Complete datasets are available through the centralized data management system.

Acknowledgements

Adarsh Jain and Christian Marcks contributed equally to this work and share first authorship. AJ appreciates the International Max Planck Research School (IMPRS) Recharge graduation school for support as well as the Interdisciplinary Center for Analytics on the Nanoscale (ICAN) for providing analytical measurement support. Authors acknowledge the financial support from the Federal Ministry of Education and Research (PrometH_2eus project in the framework of H_2Giga, funding numbers are 03HY105F, 03HY105A, 03HY105B and 03HY105E). DS is thankful for support by the Mercator Research Center Ruhr (MERCUR.Exzellenz, 'DIMENSION' Ex-2021-0034), DS acknowledge MAT4HY.NRW Consortium for cooperative support. JJ and MFT thank John-Tommes Krzeslack and Teresa Stamm for their help with XPS and Raman measurements, respectively. LG thank Deutsche Forschungsgemeinschaft (DFG, German Research Foundation) – IRTG 2803 – 461605777 for the financial support, VV thank university of Duisburg-Essen for Postdoc Seed Funding and Open Access funding enabled and organized by Projekt DEAL.

References

[1] a) M. Younas, S. Shafique, A. Hafeez, F. Javed, F. Rehman, *Fuel* **2022**, *316*, 123317; b) S. Öberg, M. Odenberger, F. Johnsson, *Applied Energy* **2022**, *328*, 120233.

[2] K. Dastafkan, Y. Li, Y. Zeng, L. Han, C. Zhao, *J. Mater. Chem. A* **2019**, *7*, 15252.

[3] R. Xu, D. Zhu, K. Du, D. Cui, H. Feng, W. Hao, D. Tian, Y. Du, *Materials Today Energy* **2022**, *25*, 100961.

[4] a) I. W. Park, J. M. Ribe, M. Fernandino, C. A. Dorao, *Adv Materials Inter* **2023**, *10*; b) L. C. de Morais, R. Bernardes-Filho, O. B. G. Assis, *World J Microbiol Biotechnol* **2009**, *25*, 123; c) L. Ru, C. Jie-rong, *Applied Surface Science* **2006**, *252*, 5076; d) K. J. Kubiak, M. Wilson, T. G. Mathia, P. Carval, *Wear* **2011**, *271*, 523.

[5] a) L. Jianxin, L. Zongqi, Z. Xiaolei, H. Gulizhaina, C. Xuedi, *International Journal of Hydrogen Energy* **2023**, *48*, 26629; b) Q. Li, Y. He, L. Zhang, W. Sun, Z. Ma, L. Zhu, Q. Lian, S. Tang, L. Pan, *Journal of Power Sources* **2024**, *606*, 234554; c) H. Altaf, N. Vorhauer, E. Tsotsas, T. Vidaković-Koch, *Processes* **2020**, *8*, 362; d) S. Bhaskaran, D. Pandey, V. K. Surasani, E. Tsotsas, T. Vidakovic-Koch, N. Vorhauer-Huget, *International Journal of Hydrogen Energy* **2022**, *47*, 31551.

[6] R. Iwata, L. Zhang, K. L. Wilke, S. Gong, M. He, B. M. Gallant, E. N. Wang, *Joule* **2021**, *5*, 887.

[7] J. Heinrich, F. Ränke, K. Schwarzenberger, X. Yang, R. Baumann, M. Marzec, A. F. Lasagni, K. Eckert, *Langmuir : the ACS journal of surfaces and colloids* **2024**, *40*, 2918.

[8] L. Krause, K. Skibińska, H. Rox, R. Baumann, M. M. Marzec, X. Yang, G. Mutschke, P. Żabiński, A. F. Lasagni, K. Eckert, *ACS applied materials & interfaces* **2023**, *15*, 18290.

[9] G. Sakuma, Y. Fukunaka, H. Matsushima, *International Journal of Hydrogen Energy* **2014**, *39*, 7638.

[10] J. Zawala, D. Kosior, *Minerals Engineering* **2016**, *85*, 112.

[11] a) J. Qin, H. Lu, *Environmental science and pollution research international* **2023**, *30*, 91591; b) A. Samanta, Q. Wang, S. K. Shaw, H. Ding, *Materials & Design* **2020**, *192*, 108744.

[12] S. Banerjee, *Simple derivation of Young, Wenzel and Cassie-Baxter equations and its interpretations*, arXiv, **2008**.

[13] D. Murakami, H. Jinnai, A. Takahara, *Langmuir : the ACS journal of surfaces and colloids* **2014**, *30*, 2061.

[14] A. Jain, C. Marcks, L. Grebener, J. Johny, A. S. Odungat, M. Chatwani, M.-A. Kräenbring, A. Shaji, M. F. Tesch, A. K. Mechler et al., *Adv Funct Materials* **2025**.

[15] P. Gerschel, S. Angel, M. Hammad, A. Olean‐Oliveira, B. Toplak, V. Chanda, R. Martínez‐Hincapié, S. Sanden, A. R. Khan, Da Xing et al., *Carbon Energy* **2024**, *6*.

[16] F. T. Haase, A. Rabe, F.-P. Schmidt, A. Herzog, H. S. Jeon, W. Frandsen, P. V. Narangoda, I. Spanos, K. Friedel Ortega, J. Timoshenko et al., *Journal of the American Chemical Society* **2022**, *144*, 12007.

[17] G. Y. Abo El-Reesh, A. A. Farghali, M. Taha, R. K. Mahmoud, *Scientific reports* **2020**, *10*, 587.

[18] S. Bapat, S. O. Kilian, H. Wiggers, D. Segets, *Nanoscale advances* **2021**, *3*, 4400.

[19] S. Bapat, D. Segets, *ACS Appl. Nano Mater.* **2020**, *3*, 7384.

[20] a) S. Shukla, S. Bhattacharjee, A. Z. Weber, M. Secanell, *J. Electrochem. Soc.* **2017**, *164*, F600-F609; b) H. Ren, X. Meng, Y. Lin, Z. Shao, *Journal of Power Sources* **2022**, *517*, 230698.

[21] A. Jain, V. Vinayakumar, A. Olean‐Oliveira, C. Marcks, M. Chatwani, A. K. Mechler, C. Andronescu, D. Segets, *ChemCatChem* **2024**, *16*.

[22] a) C. Aberle, M. Lewis, G. Yu, N. Lei, J. Xu, *Soft Matter* **2011**, *7*, 11314; b) M. Muzibur Rahman, A. Mohamed Asiri (Eds.) *Advances in Colloid Science*, IntechOpen,

2016; c) R. Chen, L. Zhang, D. Zang, W. Shen in *Advances in Colloid Science* (Eds.: M. Muzibur Rahman, A. Mohamed Asiri), IntechOpen, **2016**; d) B. Sobac, D. Brutin, *Physical review. E, Statistical, nonlinear, and soft matter physics* **2012**, *86*, 21602.
[23] H. Hu, S. Wageh, A. A. Al-Ghamdi, S. Yang, Z. Tian, B. Cheng, W. Ho, *Applied Surface Science* **2020**, *511*, 145570.
[24] C. Andronescu, S. Seisel, P. Wilde, S. Barwe, J. Masa, Y.-T. Chen, E. Ventosa, W. Schuhmann, *Chemistry (Weinheim an der Bergstrasse, Germany)* **2018**, *24*, 13773.
[25] L. Grebener, A. S. Odungat, Y. Zhu, O. Pasdag, I. Radev, E. Nürenberg, A. Kubina, V. Peinecke, S. Kohsakowski, D. Segets et al., *Journal of Power Sources* **2025**, *635*, 236457.
[26] a) S. Favero, I. E. L. Stephens, M.-M. Titirci, *Advanced materials (Deerfield Beach, Fla.)* **2024**, *36*, e2308238; b) A. Raut, H. Fang, Y.-C. Lin, S. Fu, D. Sprouster, R. Shimogawa, A. I. Frenkel, C. Bae, J. C. Douglin, J. Lillojad et al., *Angewandte Chemie International Edition* **2023**, *62*, e202306754.
[27] M. B. Karimi, F. Mohammadi, K. Hooshyari, *International Journal of Hydrogen Energy* **2019**, *44*, 28919.
[28] N. Yusoff in *Graphene-Based Electrochemical Sensors for Biomolecules*, Elsevier, **2019**, pp. 155–186.
[29] H. Si, C. Han, Y. Cui, S. Sang, K. Liu, H. Liu, Q. Wu, *Journal of Solid State Chemistry* **2021**, *295*, 121943.
[30] N. Thissen, J. Hoffmann, S. Tigges, D. A. M. Vogel, J. J. Thoede, S. Khan, N. Schmitt, S. Heumann, B. J. M. Etzold, A. K. Mechler, *ChemElectroChem* **2024**, *11*.
[31] C. Gohlke, J. Gallenberger, N. Niederprüm, H. Ingendae, J. Kautz, J. P. Hofmann, A. K. Mechler, *ChemElectroChem* **2024**.
[32] a) J. Bico, U. Thiele, D. Quéré, *Colloids and Surfaces A: Physicochemical and Engineering Aspects* **2002**, *206*, 41; b) D. Quéré, *Physica A: Statistical Mechanics and its Applications* **2002**, *313*, 32.
[33] a) Y. J. Kim, A. Lim, J. M. Kim, D. Lim, K. H. Chae, E. N. Cho, H. J. Han, K. U. Jeon, M. Kim, G. H. Lee et al., *Nature communications* **2020**, *11*, 4921; b) X. Wang, Z. Wu, J. Wei, B. Sundén, *International Journal of Heat and Mass Transfer* **2019**, *132*, 699.
[34] a) Y. Liu, S. Li, H. Wu, Y. Shi, *DeCarbon* **2024**, *5*, 100052; b) F.-M. Chang, Y.-J. Sheng, S.-L. Cheng, H.-K. Tsao, *Applied Physics Letters* **2008**, *92*.
[35] J. Qin, D. Zhou, B. Shi, F. Chen, L. Luo, A. Kumar, C. Wang, X. Lin, S. Sheng, W. Xu et al., *Langmuir : the ACS journal of surfaces and colloids* **2020**, *36*, 11422.

Supporting Information

Wetting Across the Lyophilic–Lyophobic Spectrum: Morphological Tuning of Anode Layers for the Alkaline Oxygen Evolution Reaction

*Adarsh Jain, Christian Marcks, Gereon Mahler, Ahammed Suhail Odungat, Lars Grebener, Jacob Johny, Mohit Chatwani, Abhishek Shaji, Tobias Melchert, Marc Frederic Tesch, Malte Behrens, Anna K. Mechler, Vineetha Vinayakumar, Doris Segets**

S1. Ink formulation

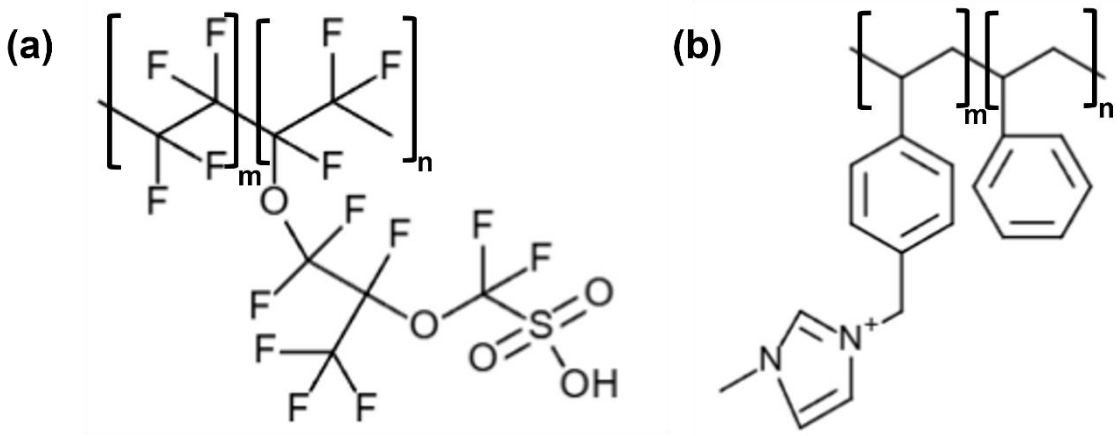

Figure S1 Molecular structure of (a) Nafion and (b) Sustainion X37-50.[1]

To understand physisorption or chemisorption of binders on the catalyst surface, a design of experiments (DoE) approach was implemented, to systematically study the influence of catalyst-to-solvent ratio (C/S), binder-to-catalyst ratio (B/S), and type of binder on the relative sedimentation time (RST). The variable factors and the experimental design is summarized in Table S1. A general full factorial design with two replicates was used for comprehensive analysis.

Table S1. Design of experiments parameters including type of binders, catalyst-to-solvent (C/S) ratio, and binder-to-catalyst (B/C) ratio along with their resulting relative sedimentation time at bulk sedimentation (RST).

Experiments	Type of binders	C/S ratio	B/C ratio	RST × 10^{15} [m^{-2}]
1	Nafion	1	0	3.29
2	Nafion	1	0.2	4.58
3	Nafion	1	0.5	7.23
4	Nafion	1	1	4.59
5	Nafion	2	0	13.80
6	Nafion	2	0.2	7.86
7	Nafion	2	0.5	11.21
8	Nafion	2	1	9.27
9	Nafion	5	0	80.43
10	Nafion	5	0.2	4.53
11	Nafion	5	0.5	4.53
12	Nafion	5	1	7.01
13	Sustainion	1	0	4.53
14	Sustainion	1	0.2	4.53
15	Sustainion	1	0.5	7.01
16	Sustainion	1	1	11.42
17	Sustainion	2	0	11.31
18	Sustainion	2	0.2	13.90
19	Sustainion	2	0.5	11.42
20	Sustainion	2	1	4.68
21	Sustainion	5	0	80.43
22	Sustainion	5	0.2	54.87
23	Sustainion	5	0.5	115.35
24	Sustainion	5	1	4.68
25	Nafion	1	0	6.90
26	Nafion	1	0.2	7.22
27	Nafion	1	0.5	7.23
28	Nafion	1	1	6.58
29	Nafion	2	0	10.68
30	Nafion	2	0.2	9.05
31	Nafion	2	0.5	7.76
32	Nafion	2	1	6.79
33	Nafion	5	0	67.17
34	Nafion	5	0.2	29.75
35	Nafion	5	0.5	19.62
36	Nafion	5	1	17.25
37	Sustainion	1	0	6.90
38	Sustainion	1	0.2	4.64
39	Sustainion	1	0.5	4.53
40	Sustainion	1	1	4.48
41	Sustainion	2	0	10.68
42	Sustainion	2	0.2	13.90
43	Sustainion	2	0.5	13.79

Experiments	Type of binders	C/S ratio	B/C ratio	RST × 10^{15} [m^{-2}]
45	Sustainion	5	0	67.17
46	Sustainion	5	0.2	200.09
47	Sustainion	5	0.5	61.66
48	Sustainion	5	1	8.51

Contour plots in Figure S2e-f show the RST empirically fitted as a function of B/C and C/S. From the dominant brown regions, it becomes clear that both Sustainion and Nafion exhibit a minimal influence on RST at low C/S ratios (≤ 2), even with elevated B/C (≤ 1). These results confirm that at C/S =1(utilized in this work's ink formulation), the addition of binder does not lead to significant chemisorption or physisorption. Beyond this range, particularly at elevated values of both C/S and B/C ratios, a marked increase in RST is observed. This trend suggests enhanced interparticle and particle–binder interactions, likely arising from increased binder adsorption and potential steric or electrostatic stabilization. Under these concentrated conditions, the higher probability of particle crowding and polymer-mediated bridging contributes to colloidal network formation, thereby retarding sedimentation and increasing RST. Compositions with elevated B/C and low C/S ratios do not exhibit increased RST, despite the presence of binder. This behavior can be attributed to the dominant role of the continuous phase in sedimentation under dilute conditions. At low C/S, the catalyst particles are sufficiently dispersed, and their settling behavior is primarily governed by solvent viscosity and volume fraction, rather than by interfacial interactions.

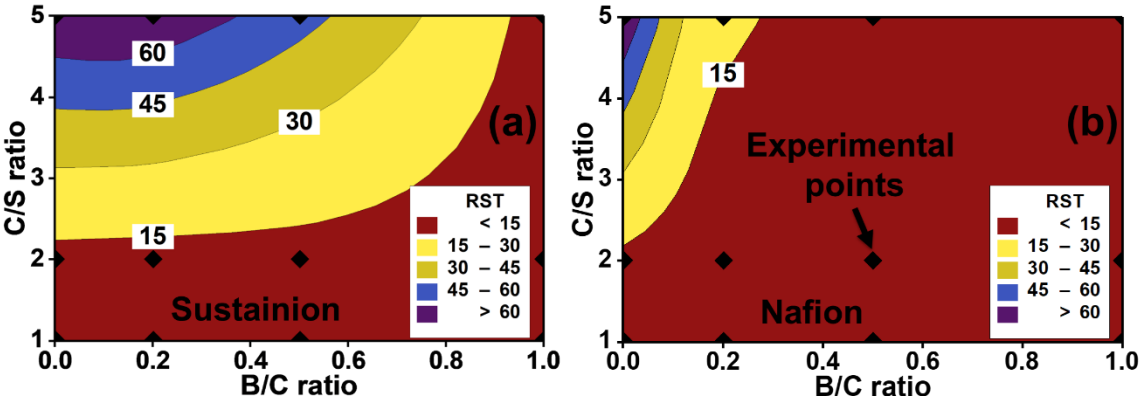

Figure S2. Visualization of the ink optimization by varying the C/S and B/C ratio along with their resulting relative sedimentation time at bulk sedimentation (RST × 10^{15} m^{-2}) as contour plot for the addition of (a) Sustainion, and (b) Nafion as binder.

S2. Layer formation and MSDQ development

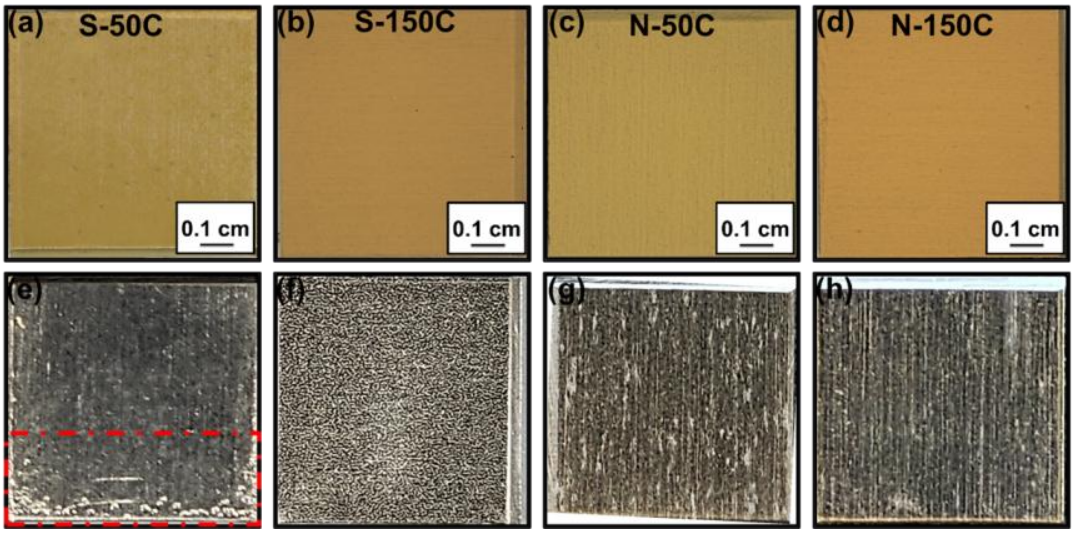

Figure S3. Optical microscopy images of spray-coated layers: (a) S-50C, (b) S-150C, (c) N-50C and (d) N-150C. Binder solution dissolved in the continuous phase coated onto Ni plate: (e) S-50C, (f) S-150C, (g) N-50C and (h) N-150C. Binder assemblages at the corner of the anode support is highlighted with red box.

The MSDQ framework was utilized to understand the quality of coatings in nanoscale within the anode surface.[21] In brief, MSDQ is a statistical approach which involves calculation of optimal number of regions of selection (ROS) measurements, followed by distribution of these ROS fairly and equally based on the periphery rule and eventually extract the surface features of the anode layer. The parameters found in MSDQ are summarized in Table S2.

Table S2. Parameters found in MSDQ: Homogeneity score (H_s) at different regions of selection (ROS), standard deviation (σ), margin of error (E), confidence interval (α) and optimal number of ROS (x) for N-50C, N-150C and S-150C anodes.

Parameters	N-50C	N-150C	S-150C
$H_{s\,(ROS1)}$ /-	0.59	0.54	0.10
$H_{s\,(ROS2)}$ /-	0.61	0.41	0.18
$H_{s\,(ROS3)}$ /-	0.53	0.49	0.14
$H_{s\,(ROS4)}$ /-	0.47	0.48	0.13
σ /-	0.065	0.054	0.087
E /%	5	5	5
α /%	95	95	90
x /-	11	10	11

3. Force balance on a bubble adhering to the anode surface

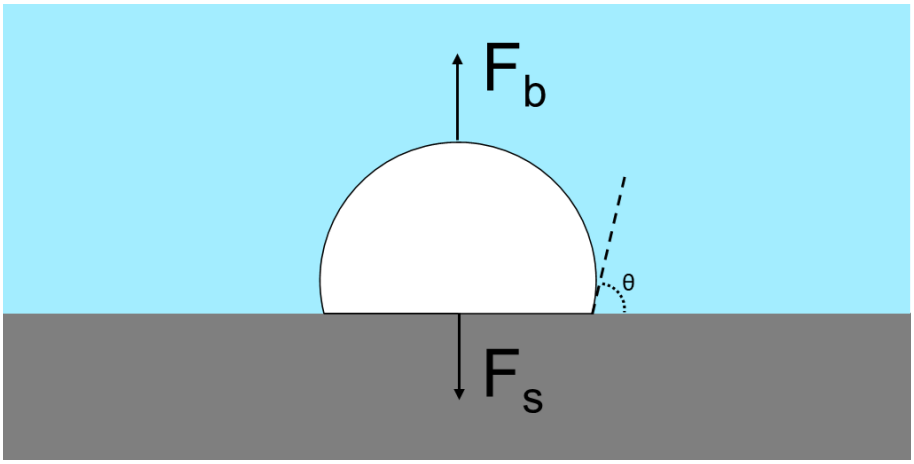

Figure S4. Force balance scheme for detaching gas bubbles considering buoyancy and surface tension forces. Adapted freely from Iwata et al., and Wang et al.[2,3]

S4. Experimental section

Ink characterization

All inks were characterized by utilizing analytical centrifugation (Analytical Centrifuge LUMisizer 6514–44, LUM GmbH). Samples of 410 µL were filled into polycarbonate (PC) tubes and placed inside the centrifuge. All measurements were conducted at 2500 RPM and 20 °C. The captured fingerprints were then converted into transmittograms for improved understanding and comparison.

Layer fabrication

The inks were deposited onto Ni plates (99.2%, HMW Hauner, 1 cm² projected area) using an ultrasonic spray coater (Sono-Tek Co., NY). Prior to coating, the Ni supports were cleaned through a chemical etching process in a 1 M HCl solution for 5 minutes, followed by rinsing with acetone and then isopropanol, each for 5 minutes, in a sonication bath (Elmasonic S 30 H, Germany) at ambient temperature. The inks were applied at a constant flow rate of 0.4 ml/min, with a total of 80 layers being deposited. For uniform coating, the initial layer was sprayed horizontally across the plate. Subsequently, the spray direction was adjusted by 90 degrees, and the next layer was applied perpendicularly to the previous one. This alternating pattern continued until all 80 layers were completed. The final mass loading was assessed using a precision balance by using the A&D BM-22 microbalance, with the coatings achieving loadings of approximately 415±34 µm/cm².

Layer characterization

A morphological analysis was conducted using SEM analysis by a Hitachi Tabletop TM3030 scanning electron microscope. Surface topography measurements were obtained through atomic force microscopy (AFM, TOSCA 400, Anton Paar Germany GmbH) using in-house-developed MSDQ.

For determination of pore coverage, the anode layer on Ni plate was mounted on a SEM sample holder using copper tape. A Helios NanoLab 600i SEM with a focused ion beam (FIB) was employed for cross-section imaging. A protective platinum line (15 µm x 0.5 µm, 0.5 µm thick) was deposited to shield the structure from high-energy FIBs. A rectangular area (15 µm x 15 µm) adjacent to the platinum line was selected, and a 5 µm deep hole was created using a 6.5 nA FIB beam current. The undamaged wall beneath the platinum deposition was polished with lower current ion beams (up to 93 pA) to obtain a smooth cross-section. Finally, images at various resolutions were captured using the SEM. The images obtained from the FIB-SEM device were processed using a MATLAB R2022a algorithm. The algorithm enhances image contrast to distinguish catalyst particles from pores, and then binarizes the images into black (catalyst) and white (pores) pixels.

To quantify the adherence and coherence of the coatings under tensile stress, the centrifugal adhesion analyzer LUMiFrac® from the company LUM has been employed. For this method, the samples have to be prepared appropriately. First, the catalyst coated Ni support was glued to a stainless steel backplate and on the top of the anode layer a copper test mass with a round adapter of 10 mm diameter was placed using an acrylic adhesive tape with a PET backbone (Lohmann DuploCOLL 362.2). Thus, the sample was in between the backplate and the test mass. In the second step, the specimen was placed in tight clamps for 24 h at room temperature to ensure that the pressure sensitive adhesive was at its peak strength. Finally, the specimen was inserted into an aluminum guiding sleeve, such that the copper test mass is always at a 90° angle to the backplate and the Ni support. This assembly was placed into a detector on a centrifugal plate. The detector identified the frequency of rotation, at which the copper test mass breaks off from the coating. From this, the adherence has been calculated.

Contact angle measurements were performed using OCA15PRO equipment (Data Physics Instruments GmbH). The measurements were conducted with 1 M KOH as the liquid which was dropped at a drop-eject-rate of 5µL s^{-1}.

XPS measurements were performed on the S-150C, N-50C, and N-150C anodes, employing a near ambient pressure XPS (SPECS GmbH) equipped with a Mg-Kα source that produces X-rats of energy 1253.6 eV. While the survey scans were recorded using a pass energy of 100 eV, high resolution scans of all desired elements such as Ni and F were recorded applying a pass energy of 20 eV at a resolution of 0.05 eV. Data analysis was performed using the CasaXPS software and peak deconvolutions were performed by applying a Shirley-type background.

Raman analysis was conducted on the Ni-Fe-LDH layers using a DXR Raman microscope from Thermo Scientific at an excitation line of 780 nm. A laser power of 10 mW was applied to collect the Raman spectra.

Electrochemical characterization

The fabricated layers were employed as working electrodes (WE) in a three-electrode beaker cell setup. For this, a Ni rod (99.5% trace metal base, HMW Hauner) with a 1 mm groove was employed as a current collector for the WEs. A miniRHE (Gaskatel GmbH) and an expanded Ni mesh (De Nora) were employed as reference and counter electrodes, respectively. The former's potential was regularly tracked vs. a true RHE.[4] 200 ml of 1 M KOH (TH Geyer) was employed as electrolyte, whereas iron (diluted in HNO_3, Agilent) was added to reach a controlled concentration of 200 ppb for every batch. Electrolyte stirring of 100 rpm was applied during the measurements.

Gamry Interfaces 1010E and Ref3000 were employed as potentiostats/galvanostats equipped with Gamry Framework Data Acquisition Software Version 7 for controlling the electrochemical measurements. The same electrochemical protocol was employed for every sample, consisting of eight main steps that will be briefly discussed here. A detailed description of the respective steps and chosen values is given in Figure S5 and Table S3.

The protocol starts with the conditioning of the anodes by cycling the potential 50 times from 0.25 to 1.5 V vs. RHE. This step is followed by determining the capacitive charge, by applying rapid CV cycling with increasing scan rates (5, 10, 25, 50, 100, 200, 400, 800 mVs^{-1}, 5 cycles each). To assess the activity and stability change of the samples, four repetitions of the following three protocol steps were applied. First, the dynamic activity of the samples is measured by cycling the potential between 1-1.8 V vs. RHE three times ("Activity") followed by stationary polarization (SP) of the anodes. For the SP, the current was measured for 180 s

at consecutive potentials of 1, 1.1, 1.2, 1.3, 1.4, 1.45, 1.5, 1.55, 1.6, 1.65, 1.7, 1.75 and 1.8 V vs. RHE. The final step in the cycles consisted of a 2 h chronopotentiometric (CP) measurement at 100 $mAcm^{-2}$ ("Stability"). After the final cycle, the capacitive charge is determined with the same procedure as explained above. Before every protocol step, the uncompensated resistance (R_u) was determined via potentiostatic electrochemical impedance spectroscopy (PEIS) at open circuit potential (AC voltage 10 mV rms, 300 kHz -1 kHz, 10 points per decade). R_u was determined at the lowest absolute difference from the PEIS-phase from zero. All protocol steps were corrected with 100 % of their respective R_u value.

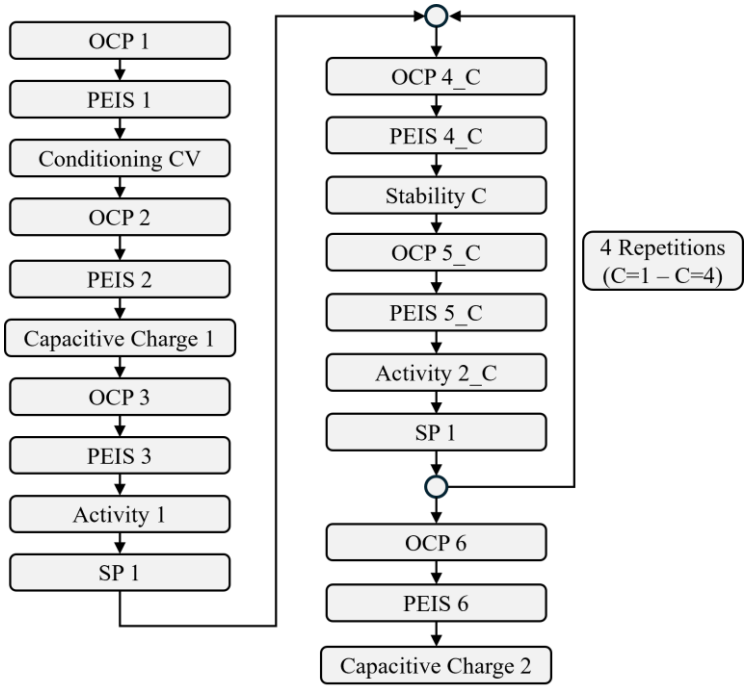

Figure S5. Detailed electrochemical protocol. The specific values for every step are displayed in Table S3.

Table S3. Protocol settings for the single steps of the electrochemical protocol, as displayed in Figure S5.

Protocol step	Specifications
OCP 1 – OCP 6	180s
PEIS 1 – PEIS 6	DC voltage: preceding OCP value, AC voltage: 10 mV rms, 300000 Hz-1000 Hz, 10 points per decade
Conditioning CV	0.25 V – 1.5 V vs. RHE, 100 mV s^{-1}, 50 cycles
Capacitive Charge 1 – Capacitive Charge 2	0.95 V – 0.85 V vs. RHE, 5 mV s^{-1}, 10 mV s^{-1}, 25 mV s^{-1}, 50 mV s^{-1}, 100 mV s^{-1}, 200 mV s^{-1}, 400 mV s^{-1}, 800 mV s^{-1}, 5 cycles, 20 s equilibration time at 0.95 V before the first scan of a new scan rate
Activity 1 – Activity 2_4	1 V – 1.8 V vs. RHE, 5 mV s^{-1}, 3 cycles
SP 1 – SP 2_4	1 V, 1.1 V, 1.2 V, 1.3 V, 1.4 V, 1.45 V, 1.5 V, 1.55 V, 1.6 V, 1.65 V, 1.7 V, 1.75 V and 1.8 V vs. RHE, 180 s each
Stability 1 – Stability 4	Chronopotentiometry at 100 mA cm^{-2}, 2 h

References

[1] A. Raut, H. Fang, Y.-C. Lin, S. Fu, D. Sprouster, R. Shimogawa, A. I. Frenkel, C. Bae, J. C. Douglin, J. Lillojad et al., *Angewandte Chemie International Edition* **2023**, *62*, e202306754.

[2] R. Iwata, L. Zhang, K. L. Wilke, S. Gong, M. He, B. M. Gallant, E. N. Wang, *Joule* **2021**, *5*, 887.

[3] X. Wang, Z. Wu, J. Wei, B. Sundén, *International Journal of Heat and Mass Transfer* **2019**, *132*, 699.

[4] G. Jerkiewicz, *ACS Catal.* **2020**, *10*, 8409